Supplementary Information (SI) for Inorganic Chemistry Frontiers.

Supporting Information for

Magneto-Chiral Dichroism in a Chiral Twistacene Ytterbium(III) One-dimensional Assembly of Single-Molecule Magnets

Israa Shioukhi,[a] Langit Cahya Adi,[b] Vincent Dorcet,[c] Olivier Cador,[c] Geert L. J. A. Rikken,[b] Boris Le Guennic,[c] Jeanne Crassous,[c*] Cyrille Train,[b] Fabrice Pointillart,[c*] Matteo Atzori,[b*] Ori Gidron[a*]

a *Institute of Chemistry and the Center for Nanoscience and Nanotechnology, The Hebrew University of Jerusalem Edmond J. Safra Campus, 9190401 Jerusalem, Israel*

b *Laboratoire National des Champs Magnétiques Intenses (LNCMI), CNRS, Univ. Grenoble Alpes, INSA Toulouse, Univ. Toulouse Paul Sabatier, EMFL, Grenoble – France*

c *Univ Rennes, CNRS, ISCR (Institut des Sciences Chimiques de Rennes) – UMR 6226, F-35000 Rennes, France*

Contents

S1 General

Material characterization

Commercially available reagents and chemicals were used without further purification unless otherwise stated. The metal building blocks Yb(hfac)$_3$(H$_2$O)$_2$ (hfac$^-$ = 1,1,1,5,5,5-hexafluoroacetylacetonate anion) was synthesized following previous reported method.[1] The twistacenes were synthesized according to previously published methods.[2]

Chiral HPLC separations were performed with a Chiralpak® IG semi-preparative column and CHIRALPAK® IB-N (250 × 4.6 mm / 5μm) preparative columns, with hexane/dichloromethane as eluent.

^{1}H and ^{13}C NMR spectra were recorded in solution on a Bruker-Neo 500 MHz spectrometer using the ^{1}H signal of tetramethylsilane (TMS) or the residual solvent peak that had been previously calibrated to TMS as the external standard. ^{13}C-NMR spectra were referenced to the ^{1}H frequency multiplied by the standard factor of 0.25145020. ^{13}C-NMR spectra were ^{1}H decoupled. The spectra were recorded using chloroform-*d*. Chemical shifts (δ) are expressed in ppm.

UV-vis absorption spectra were recorded with an Agilent Cary-5000 spectrophotometer. The spectra were measured using a quartz cuvette (1 cm) at 25 °C. The absorption wavelengths are reported in nm with the extinction coefficient ε (M^{-1} cm^{-1}) in brackets.

Steady state fluorescence measurements were performed on a HORIBA JOBIN YVON Fluoromax-4 spectrofluorometer with the excitation/emission geometry at right angles.

Electronic Circular Dichroism (ECD) spectra were recorded on a MOS-500 spectrophotometer from BioLogic Science Instruments.

High resolution mass spectra were measured on a HR Q-TOF LCMS and Waters Micromass GCT_Premier Mass Spectrometer using ESI. All solid-state characterization studies (elementary analysis, IR, PXRD, magnetic susceptibility and photophysical measurements) were performed on dried samples and are considered without crystallization solvents. The elemental analyses of the compounds were performed at the Centre Régional de Mesures Physiques de l'Ouest, Rennes.

X-ray structure analysis. Single crystals were mounted on a D8 VENTURE Bruker-AXS diffractometer for data collection for compounds *M*- or *P*-**1** (MoKα radiation source, λ = 0.71073 Å) from the Centre de Diffractométrie X (CDIFX), Université de Rennes, France. Structures were solved with direct methods using the SHELXT Program[3] and refined with a full matrix least-squares method on F2 using the SHELXL-14/7 program.[4] A SQUEEZE procedure of PLATON[5] was performed as the structures for *M*-**1** or *P*-**1** contain large solvent accessible voids in which residual peaks of diffraction were observed. Accessible voids correspond to 3 *n*-pentane molecules of crystallization for *M*-**1** and 2.5 *n*-pentane molecules of crystallization for *P*-**1**. Crystallographic data are summarized in Table S1. Crystallographic data for the structure reported in this study have been deposited with the Cambridge Crystallographic Data Centre (insert CCDC 2390932 and 2390931 for *M*- or *P*-**1**, respectively).

Magnetic Measurements.

The direct current magnetic susceptibility measurements were performed on immobilized solid polycrystalline sample (selected single crystals) with a Quantum Design MPMS-XL SQUID magnetometer between 2 and 300 K in applied magnetic field of 10000 Oe. The alternate current magnetic susceptibility measurements were performed on a Quantum Design PPMS magnetometers for frequencies between 100 and 10000 Hz and also for the magnetization curve in dc mode at 4 K. These measurements were all corrected for the diamagnetic contribution as calculated with Pascal's constants.[6]

Computational details.

The computational procedure employed here is similar to the one used on complex *M*-**2** to allow direct comparison.[7] The models extracted from X-ray data were fully optimized excepted the first coordination sphere which was maintained fixed, by employing Kohn-Sham Density Functional Theory (DFT). The 2022.103 release of the Amsterdam Density Functional (ADF) software package was employed,[8] using the scalar all-electron zeroth-order regular approximation (ZORA)[9,10] along with the PBE (Perdew-Burke-Ernzerhof) generalized gradient approximation (GGA) functional.[11,12] For all atoms, the atomic basis set corresponded to the triple-ζ polarized (TZP) Slater-type orbital (STO) all-electron basis set.[13] Based on these geometries, multi-reference calculations have been done through the state average (SA) complete active space self-consistent field (CASSCF) approach[14] with the OpenMolcas quantum-chemistry package (version 22.10).[15,16] The active space was filled by 13 electrons spanning the seven 4*f* orbitals of the Yb^{III} ion, i.e. CAS(13,7). The second-order Douglas-Kroll-Hess scalar relativistic Hamiltonian[17-19] and the all-electron atomic natural orbital relativistic contracted (ANO-RCC) basis set from the Molcas library[20-22] were used to take into account the scalar relativistic (SR) effects. The following contractions were employed for Yb [25s22p15d11f4g2h/8s7p4d3f2g1h], for O and N [14s9p4d3f2g/4s3p2d], for C and F [14s9p4d3f2g/3s2p], and for H [8s4p3d1f/2s]. To describe the low-lying 4*f* states, all 7 SR spin-doublet states were calculated. Cholesky decomposition of the bi-electronic integrals was employed to save disk space and to speed up the calculations.[23] In order to obtain a better description of the electronic structure, calculations were computed using perturbation theory at the second order, i.e. CAS(13,7)PT2, based on the previous SA CAS(13,7)SCF descriptions.[24,25] Spin-Orbit coupling (SO) was then added within the restricted active space state interaction (RASSI) method[26,27] by mixing the wave functions and by calculating SO integrals with the atomic mean-field integrals (AMFI) approximation.[28] The *g*-factor and *ab initio* crystal-field parameters were extracted from the Single_Aniso module.[29]

Magneto-Chiral Dichroism Spectroscopy.

Magneto-Chiral Dichroism spectra were recorded with a home-made multichannel MChD spectrometer operating in the visible and near infrared spectral window (420−1600 nm) between 4.0 and 290 K with an alternating magnetic field ***B*** up to ±2 T. A detailed description of the measurement apparatus has been reported elsewhere.[29] MChD spectra were acquired on single crystals of enantiopure *M*-**1** and *P*-**1**. The samples were mounted on a titanium sample holder over a 0.5 mm hole diameter centred with respect to a 1.0 mm diameter collimated beam. Measurements were performed in the 4.0−290 K range with an alternating magnetic field ***B*** = ±1.0 T and frequency $\Omega = 0.04$ Hz. MChD spectra as a function of the magnetic field were recorded at $T = 4.0$ K for alternating magnetic fields of different amplitudes (0.25-2.0 T). Unpolarized light was provided by a broadband Energetiq – Hamamatsu Laser Driven Light Source (EQ-99X-FC-S). The spectra were collected with a high resolution/high sensitivity Optosky detector equipped with a thermoelectric cooled sensor operating in the 820−1000 nm spectral region with an analogic/digital convertor of 16 bits. Each spectrum was correlated to a specific magnetic field value by a dual channel digitizer (Picoscope 5000B) acquiring simultaneously triggers from the spectrometer and the magnetic field from a calibrated Hall effect sensor (Lakeshore) placed in proximity of the sample. Data are then post-processed as a synchronous detection with specific MatLab routines to obtain the MChD spectra.

The MChD dissymmetry factor g_{MChD} is defined as follows:

$$g_{MChD} = \frac{\Delta A_{MChD}}{A\,B} \tag{eq. S2}$$

where ΔA_{MChD} is the differential absorption of light collected under a magnetic field parallel and antiparallel oriented with respect to the light wavevector $\boldsymbol{k}$, A is the sample absorption at zero field and $\boldsymbol{B}$ is the applied magnetic field intensity.

S2 Synthesis

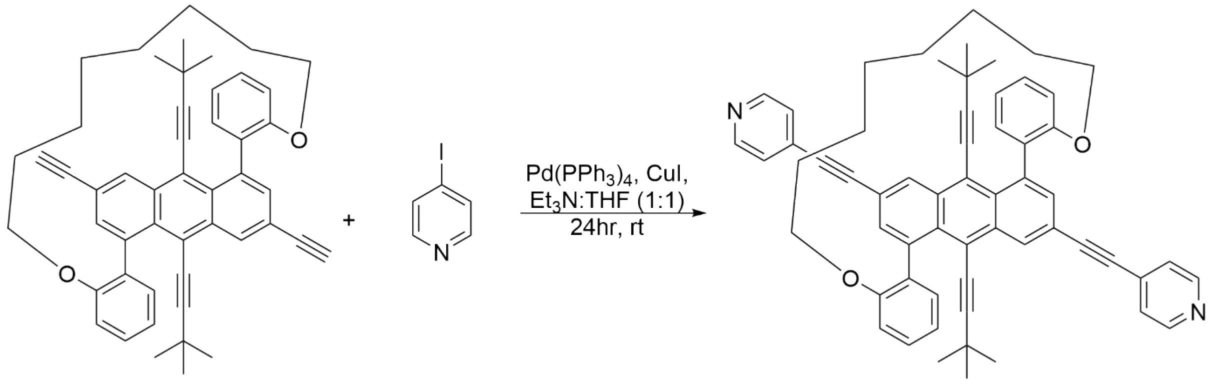

P or *M*-Ant-C8

***M* and *P*-Ant-C8**.

General procedure for the synthesis of *P* and *M* Ant-C8 ligands: Under an inert atmosphere, enantiopure twistacene-C8 (100 mg, 0.156 mmol), 4-iodopyridine (80 mg, 0.391 mmol), Pd(PPh$_3$)$_4$, (9 mg, 5% mol, 0.00783 mmol) and CuI (2.9 mg, 10% mol, 0.0156 mmol) were added to an oven-dried one-necked round bottomed flask equipped with a magnetic stirrer. A mixture (4 mL) of dry trimethylamine and tetrahydrofuran (1:1) was added to the previously mixed reagents. The reaction mixture was stirred for 24 hours at room temperature. The solvents were evaporated and the reaction mixture was loaded into a silica gel column. A 50% of a mixture of ethyl acetate in hexane was used to obtain the desired products.

Following this general procedure, *P*-Ant-C8 was obtained as a yellow solid (70 mg, 55 % yield). ^{1}H NMR (500 MHz, CDCl3) δ 8.72 (d, J = 9.2 Hz, 2H), 8.49 (s, 4H), 7.63 (d, J = 9.2 Hz, 2H), 7.50 (ddd, J = 8.2, 7.4, 1.7 Hz, 2H), 7.44 (dd, J = 7.4, 1.7 Hz, 2H), 7.12 (td, J = 7.5, 1.0 Hz, 2H), 7.00 – 6.95 (m, 6H), 3.98 – 3.91 (m, 2H), 3.81 (dt, J = 8.7, 6.1 Hz, 2H), 1.36 – 1.29 (m, 4H), 1.16 (s, 18H), 0.67 (d, J = 10.4 Hz, 2H), 0.58 – 0.50 (m, 6H). ^{13}C NMR (126 MHz, CDCl$_3$) δ 158.21, 149.61, 142.55, 135.03, 132.56, 131.86, 131.59, 130.08, 129.41, 128.28, 128.00, 125.59, 122.47, 120.23 (d, $J = 3.2$ Hz), 116.51, 112.06, 95.36, 91.86, 78.83, 69.51, 31.00, 29.73, 29.39, 28.76, 27.07. HR-ESI-MS m/z (100%): 835.4253 (100, $[M]^+$) calcd. for $C_{60}H_{56}O_2N_2^+$: 835.4258.

M-Ant-C8: Following the general procedure, *M*-Ant-C8 was obtained as a yellow solid (78 mg, 60% yield). NMR spectra of *M*-Ant-C8 are consistent the NMR spectra of compound *P*-Ant-C8.

$[Yb(hfac)_3($*M*-or*P*-Ant-C8$)]_n$ (*M*- or *P*-1). 1 equiv. (16.6 mg, 0.02 mmol) of $Yb(hfac)_3(H_2O)_2$ was dissolved in 5 mL of toluene and 1 equiv. (16.7 mg, 0.02 mmol) of *M*- or *P*-Ant-C8 was dissolved in 5 mL of toluene. The two resulting toluene solutions were mixed and stirred for 2 hours under reflux. After this delay, *n*-pentane was diffused leading to yellow single crystals that were suitable for X-ray studies. 19.6 mg, 60% yield. Anal. calcd (%) for $C_{75}H_{57}YbF_{18}N_2O_8$: C 55.24, N 1.72 H 3.50; found: C 55.62, N 1.62 H 3.65 for *M*-**1** and C 55.67, N 1.60 H 3.59 for *P*-**1**. I. R. (KBr, range 3200–500 cm^{-1}) 3061, 2946, 2865, 1655, 1555, 1528, 1506, 1256, 1201, 1147, 799, 684, 662 and 585 cm^{-1} for *M*-**1** and 3120, 3060, 2946, 2865, 1654, 1554, 1528, 1508, 1255, 1199, 1147, 800, 684, 662 and 583 cm^{-1} for *P*-**1**.

S3 Characterization

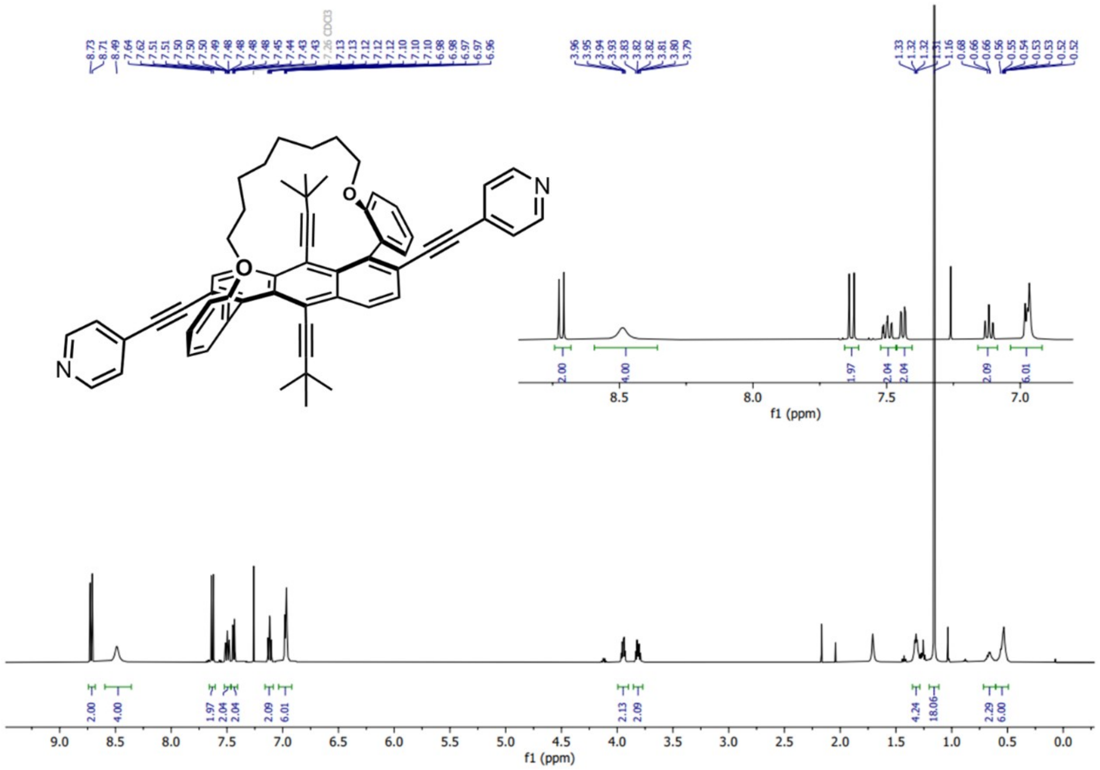

Figure S1. ^{1}H NMR (500 MHz) of *P*-Ant-C8 in $CDCl_3$, measured at 298 K.

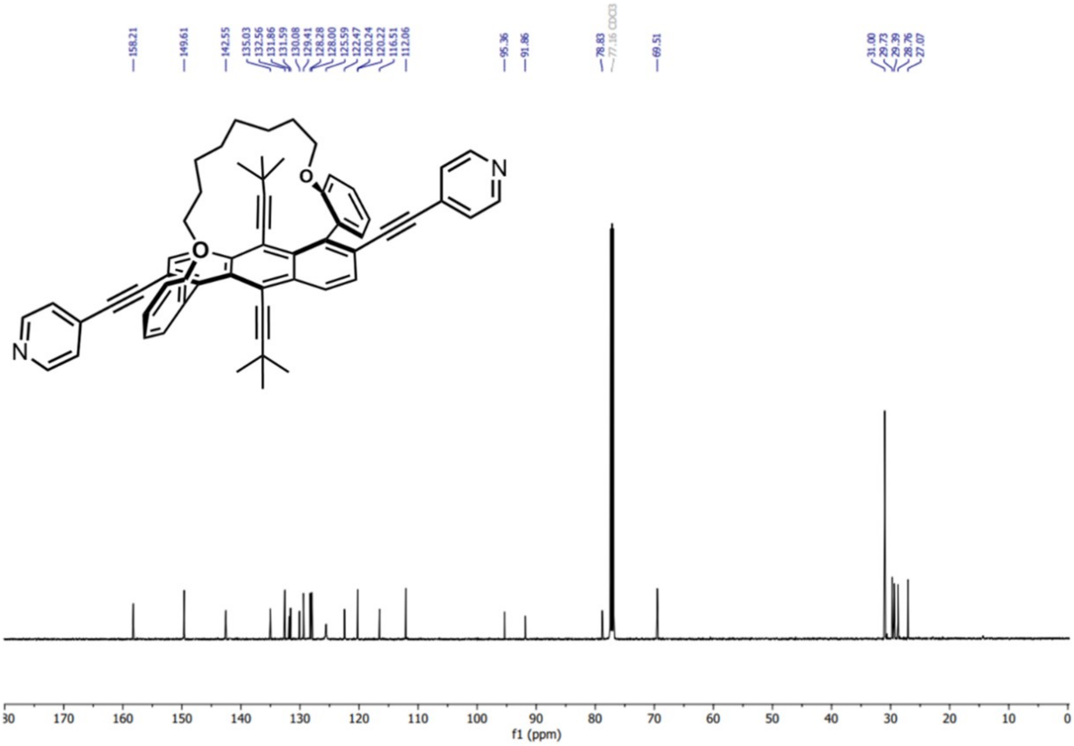

Figure S2. ^{13}C NMR (126 MHz) of *P*-Ant-C8 in $CDCl_3$, measured at 298 K.

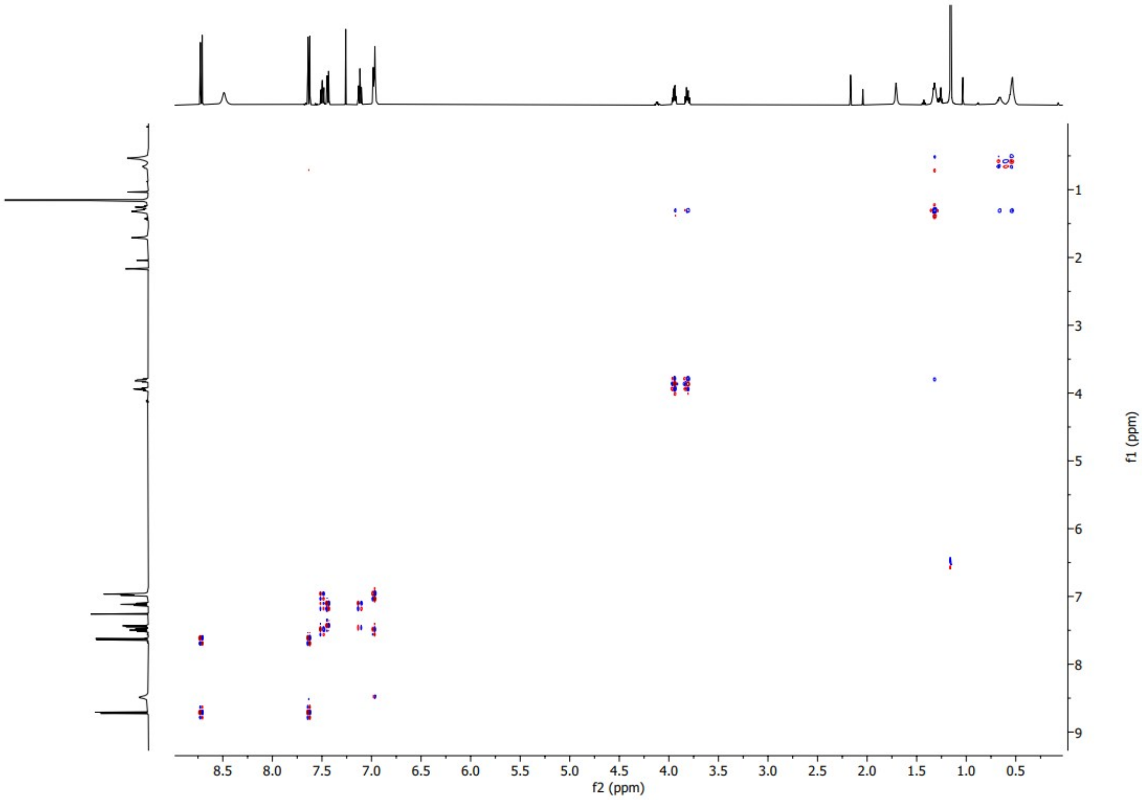

Figure S3. COSY (500 MHz) of *P*-Ant-C8 in $CDCl_3$, measured at 298 K

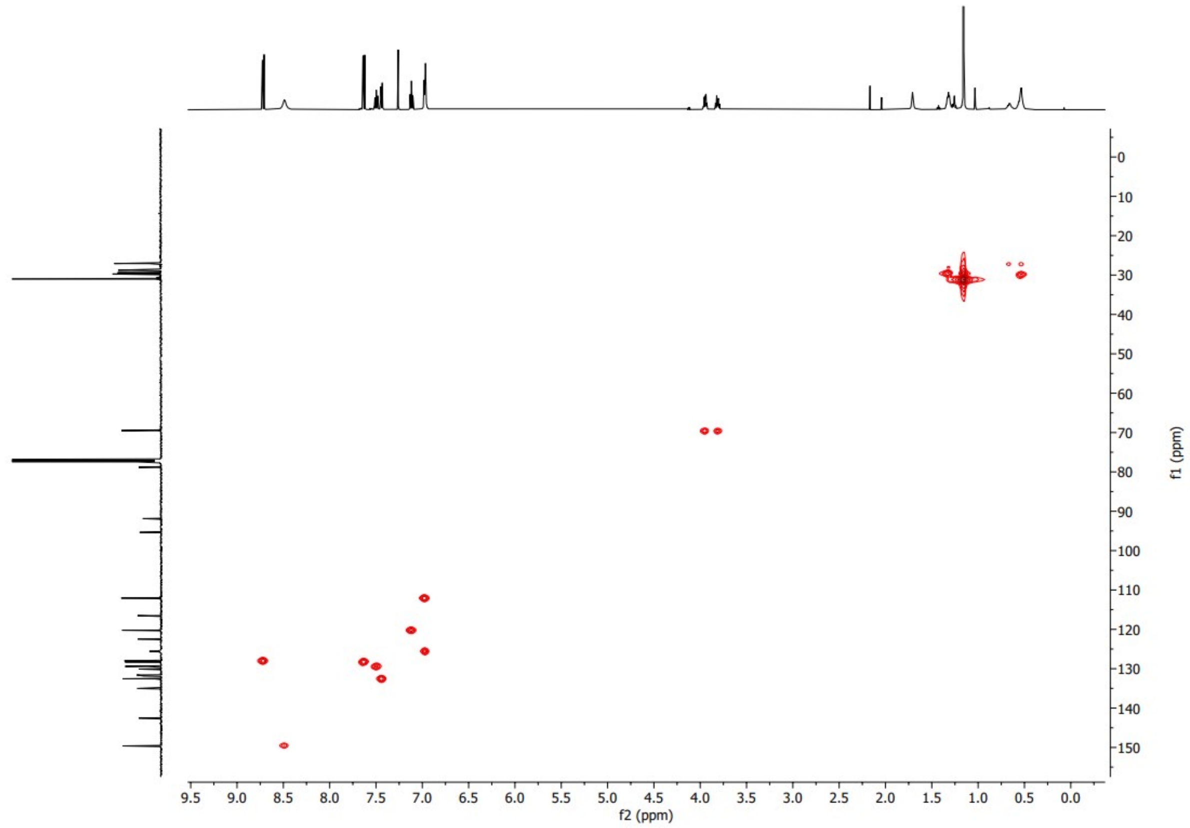

Figure S4. HSQC (**5**00 MHz) of *P*-Ant-C8 in CDCl$_3$, measured at 298 K.

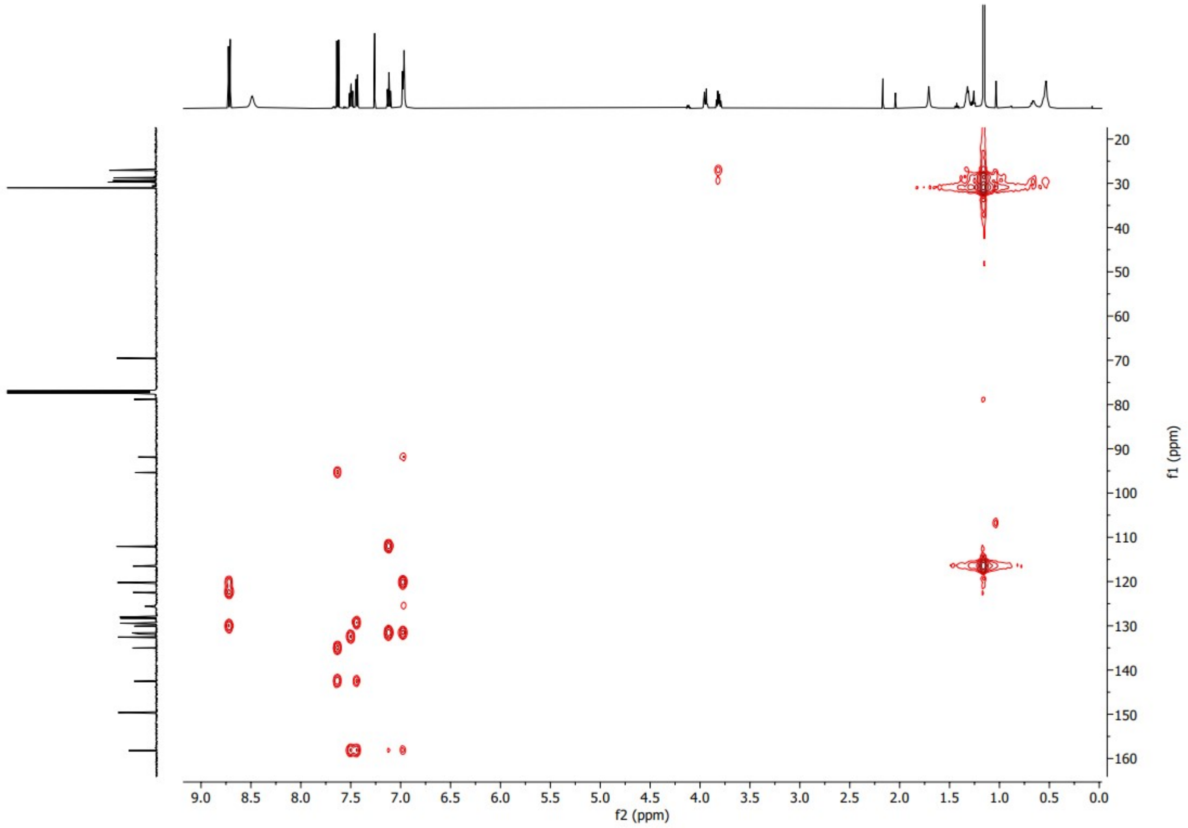

Figure S5. HMBC (500 MHz) of *P*-pyridine-C8 in CDCl$_3$, measured at 298 K.

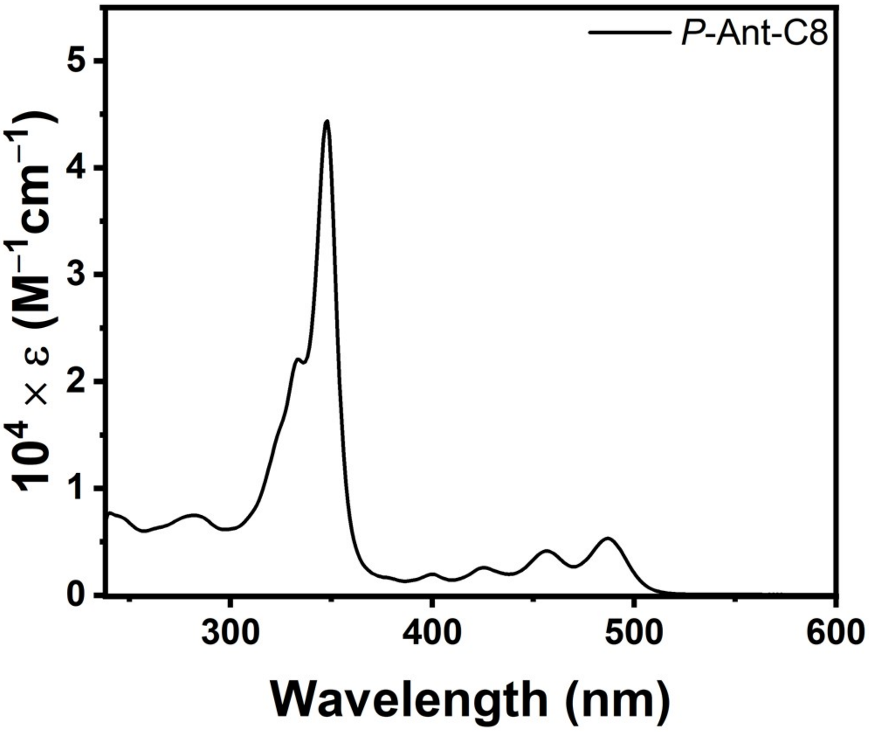

Figure S6. UV-vis absorption spectrum of *P*-Ant-C8 ligands dissolved in chloroform, and measured at 298 K.

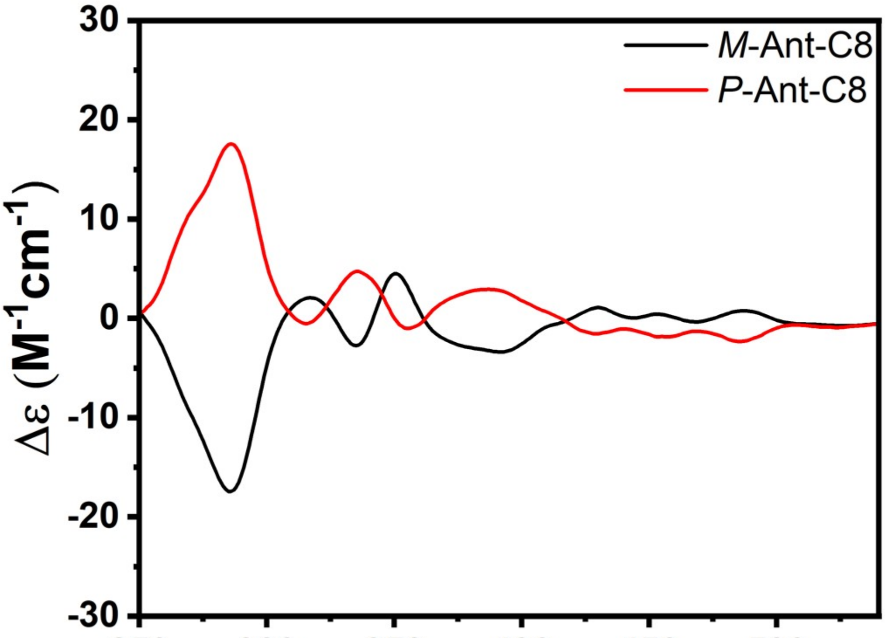

Figure S7. ECD spectra of *P* and *M* Ant-C8 ligands dissolved in chloroform and measured at 298 K.

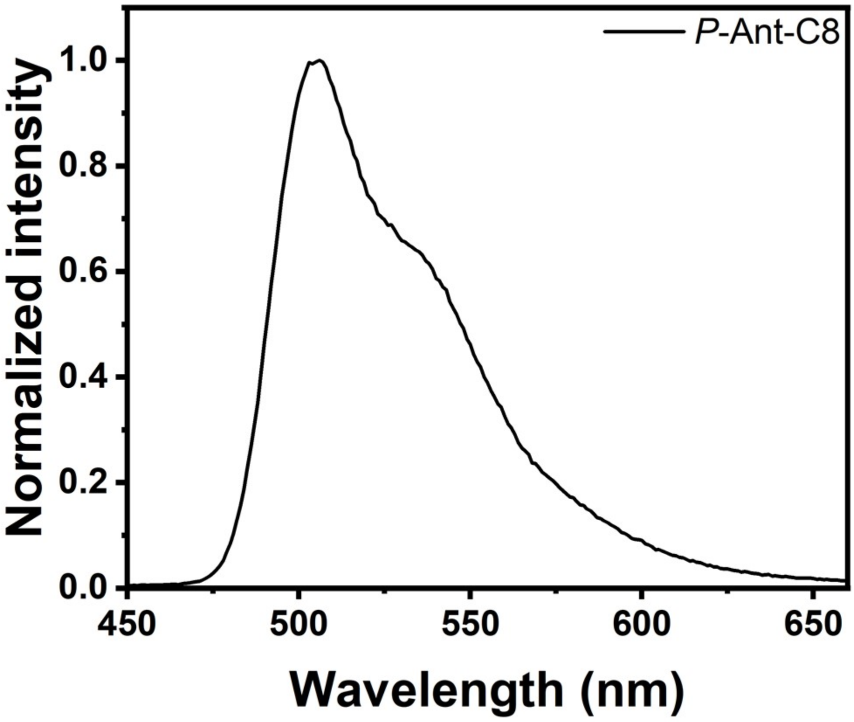

Figure S8. Emission spectrum of *P*-Ant-C8 ligands dissolved in chloroform and measured at 298 K.

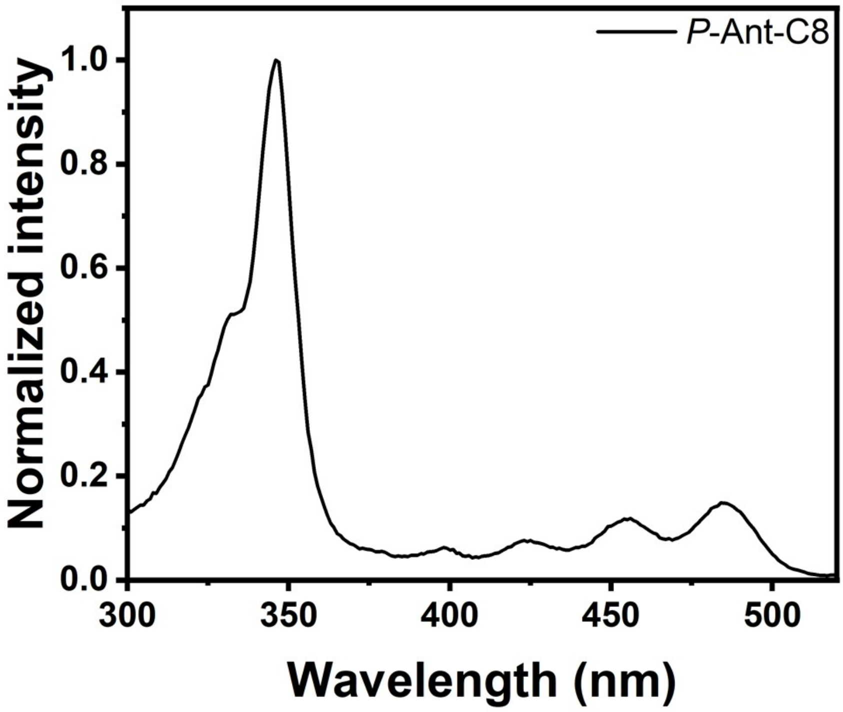

Figure S9. Excitation spectrum of *P*-Ant-C8 ligands dissolved in chloroform and measured at 298 K.

S4 Magnetic Measurements Analysis

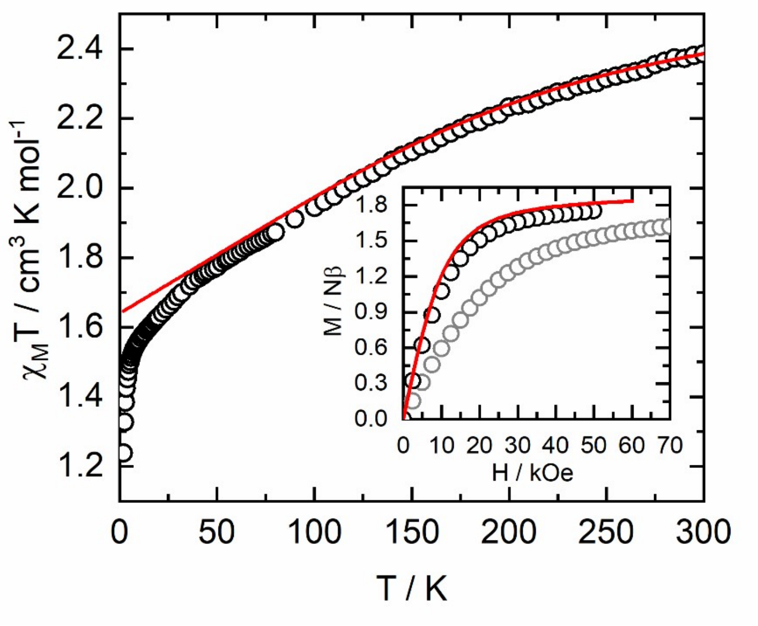

Figure S10. Thermal dependence of the product of the magnetic susceptibility by the temperature in the 2-300 K temperature range under 10 kOe dc field for *M*-**1**. In inset, field dependence of the magnetization et 2 K (open black circles) and 4 K (open gray circles). Full red lines are the calculated magnetic susceptibility and magnetization using ab initio approach (see experimental details).

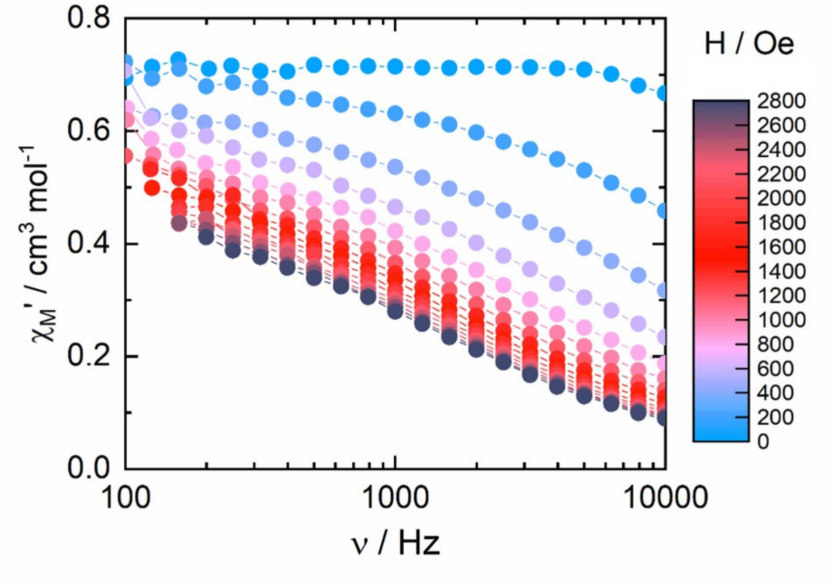

Figure S11. Frequency dependence (100−10000 Hz) of the in-phase component χ_M' of the molar magnetic susceptibility of *M*-**1** as a function of the dc magnetic field (0−2800 Oe) at T = 2.0 K.

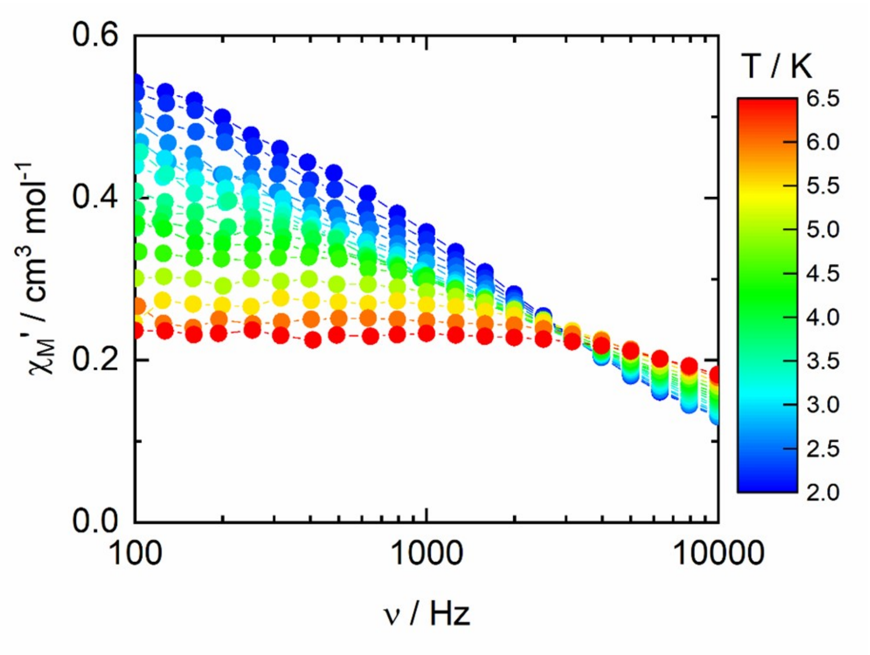

Figure S12. Frequency dependence (100−10000 Hz) of the in-phase component χ_M’ of the molar magnetic susceptibility of *M*-**1** as a function of the temperature (2−6.5 K) at H = 1400 Oe.

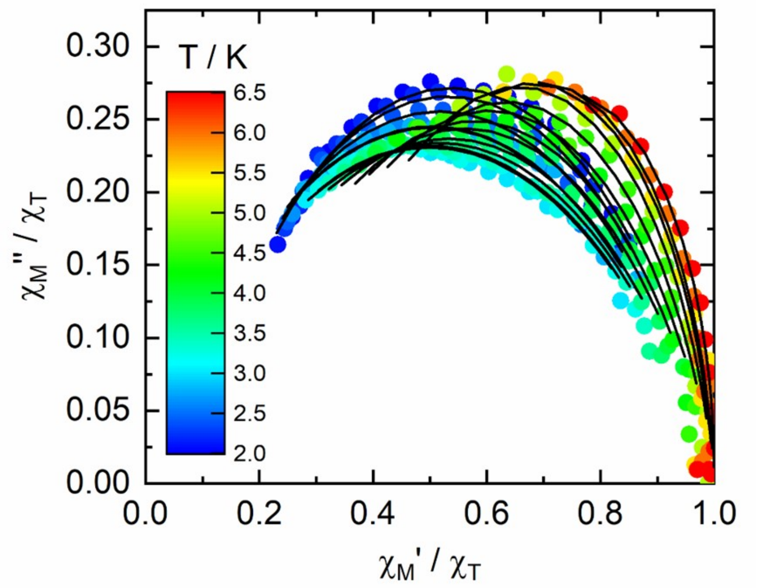

Figure S13. Normalized Cole-Cole plots for *M*-**1** at several temperatures between 2 and 6.5 K under an applied magnetic field of 1400 Oe. Full black lines are the best fits using extended Debye model detailed in the text.

S5 Magneto-chiral dichroism (MChD) analysis

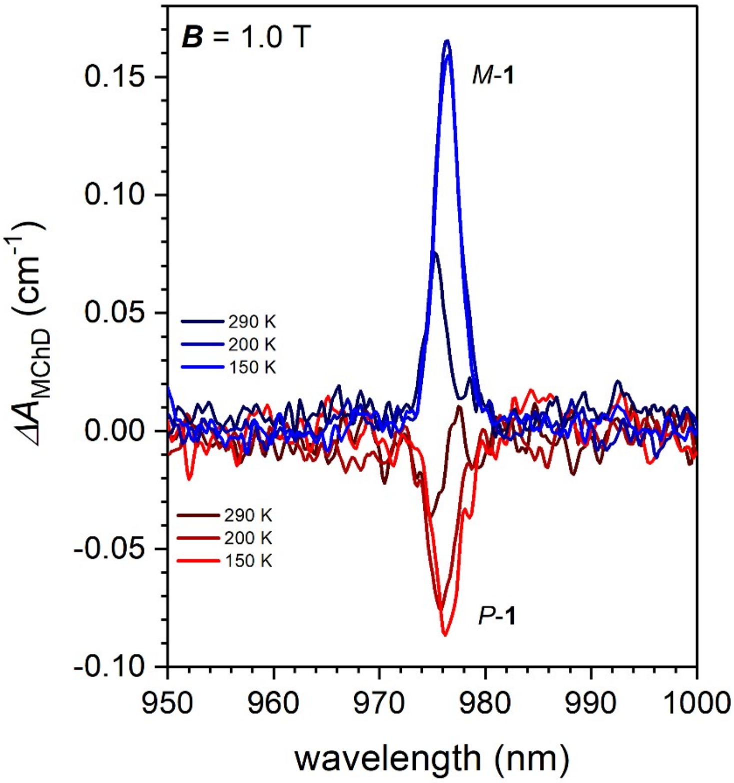

Figure S14. Temperature dependence of ΔA_{MChD} for *M*-**1** and *P*-**1** at $B = 1.0$ T in the 900-1000 nm range highlighting the residual MChD signal at room temperature.

Extended Debye model used for *M*-1 in 1400 Oe applied field at low temperature (Eq. S1).

$$\chi_M' = \chi_S + (\chi_T - \chi_S)\frac{1+(\omega\tau)^{1-\alpha}\sin\left(\alpha\frac{\pi}{2}\right)}{1+2(\omega\tau)^{1-\alpha}\sin\left(\alpha\frac{\pi}{2}\right)+(\omega\tau)^{2-2\alpha}}$$

$$\chi_M'' = (\chi_T - \chi_S)\frac{(\omega\tau)^{1-\alpha}\cos\left(\alpha\frac{\pi}{2}\right)}{1+2(\omega\tau)^{1-\alpha}\sin\left(\alpha\frac{\pi}{2}\right)+(\omega\tau)^{2-2\alpha}}$$

With χ_T the isothermal susceptibility, χ_S the adiabatic susceptibility, τ the relaxation time and α an empiric parameter which describe the distribution of the relaxation time. For SMM with only one relaxing object α is close to zero. The extended Debye model was applied to fit simultaneously the experimental variations of χ_M' and χ_M'' with the frequency ν of the oscillating field ($\omega = 2\pi\nu$). Typically, only the temperatures for which a maximum on the χ_M'' vs. ν curves, have been considered. The best fitted parameters τ, α, χ_T, χ_S are listed in Tables S5 and S6 with the coefficient of determination R^2.

S6 Crystallographic refinement parameters

Table S1. Summary of X-ray crystallographic data for *P*-**1** and *M*-**1**

Compound	*P*-**1**	*M*-**1**
Empirical formula	$C_{75}H_{57}F_{18}N_2O_8Yb$	$C_{75}H_{57}F_{18}N_2O_8Yb$
Formula weight (g /mol)	1629.26	1629.26
CCDC number	2390931	2390932
Temperature (K)	150(2)	150(2)
Wavelength (Å)	0.71073	0.71073
Crystal size (mm)	0.590 x 0.420 x 0.160	0.450 x 0.210 x 0.120
Crystal system	orthorhombic	orthorhombic
Space group	*C222*	*C222*
a (Å)	22.849(2)	22.9044(14)
b (Å)	43.262(4)	43.294(3)
c (Å)	16.8055(15)	16.8567(11)
α (°)	90	90
β (°)	90	90
γ (°)	90	90
Volume (Å^3)	16613(3)	16715.5(18)
Z	8	8
$\rho_{calculated}$ (g.cm^{-3})	1.301	1.295
Absorption coefficient (mm^{-1})	1.215	1.207
F (000)	6520	6536
Crystal colour	orange	orange
θ range for data collection (°)	2.156 to 27.483	2.060 to 27.484
Limiting indices	$-29\leq h\leq 29$ $-56\leq k\leq 56$ $-19\leq l\leq 21$	$-29\leq h\leq 29$ $-56\leq k\leq 49$ $-21\leq l\leq 21$
Reflections unique	79582	58690
Reflections collected [*I*>2s(*I*)]	12698 [R(int)^a = 0.0453]	11602 [R(int)^a = 0.0649]
Completeness to θ_max	0.993	0.998
Absorption correction type	multi-scan	multi-scan
Max. and min. transmission	0.823, 0.641	0.865, 0.649
Refinement method	Full-matrix least-squares on F^2	Full-matrix least-squares on F^2
Data / restraints / parameters	19047 / 141 / 942	19145 / 633 / 955
Goodness-of-fit on *F*2	1.036	1.032
Final *R* indices [$I>2\sigma$]	R1^c = 0.0451, wR2^d = 0.1081	R1^c = 0.0587, wR2^d = 0.1432
R indices (all data)	R1^c = 0.0767, wR2^d = 0.1289	R1^c = 0.1049, wR2^d = 0.1701
Flack parameter	0.10(3)	0.11(3)

$R1 = \Sigma||F_o|-|Fc||/\Sigma|F_o|$, $wR2 = [\Sigma[w(F_o^2-F_c^2)^2]/\Sigma[w(Fo^2)^2]]^{½}$, $w = 1/[\sigma^2(Fo^2) + (aP)^2 + bP]$,
where $P = [\max(Fo^2,0) + 2Fc^2]/3$.

Table S2. SHAPE analysis of the coordination polyhedra around the trivalent lanthanide centres in *M*-**1** and *P*-**1**.

Compounds	Centers	CShM TDD-8 (Triangular dodecahedron D_{2d})	CShM BTPR-8 (Biaugmented trigonal prism C_{2v})	CShM SAPR-8 (Square antiprism D_{4d})
M-**1**	Yb1	2.906	2.418	0.207
	Yb2	2.774	2.521	0.343
P-**1**	Yb1	2.885	2.457	0.236
	Yb2	2.844	2.515	0.268

S7 Computational Details

Table S3. Relative energies (cm^{-1}) for the ground and excited Kramers doublets (KD) of *M*-**1** for both Yb(III) centers obtained at SA-CAS(13,7)PT2/RASSI-SO level.

	KD	Yb1	Yb2
$^2F_{5/2}$	**2'**	10869	10875
	1'	10604	10667
	0'	10381	10385
$^2F_{7/2}$	**3**	586	590
	2	458	477
	1	272	345
	0	0	0

Table S4. *g*-values and m_J percentage composition of the $^2F_{7/2}$ Kramers doublets (KD) of *M*-**1** for both Yb(III) centers obtained at SA-CAS(13,7)PT2/RASSI-SO level.

	KD	g_x	g_y	g_z	$\| m_J >$ composition
Yb1	**3**	0.9	2.2	6.4	46 |±1/2> + 46 |±3/2> + 8 |±5/2>
	2	3.1	2.5	1.7	49 |±1/2> + 25 |±5/2> + 23 |±3/2>
	1	0.1	0.3	7.5	64 |±5/2> + 20 |±3/2> + 14 |±7/2>
	0	0.2	0.6	7.1	81 |±7/2> + 12 |±3/2>
Yb2	**3**	5.1	3.9	1.2	51 |±1/2> + 46 |±3/2>
	2	0.4	1.3	3.2	38 |±1/2> + 30 |±5/2> + 29 |±3/2>
	1	0.4	0.7	7.3	66 |±5/2> + 18 |±3/2> + 9 |±7/2>
	0	0.2	0.4	7.3	87 |±7/2>

Table S5. Fit parameters (χ_T, χ_S, τ and α) with the extended Debye model for the compound *M*-**1** at 2 K in the magnetic field range 200-2800 Oe.

H / Oe	χ_T / cm^3 mol^{-1}	χ_S / cm^3 mol^{-1}	τ / s	α	R^2
200	0.14491	0.41743	1.92902E-5	0.42204	0.99938
400	0.08184	0.39213	3.92493E-5	0.414	0.99962
600	0.04789	0.37965	5.9978E-5	0.40675	0.99946
800	0.0369	0.36084	7.63535E-5	0.3778	0.99939
1000	0.02431	0.36081	9.48825E-5	0.393	0.99866
1200	0.02057	0.34723	1.0424E-4	0.37602	0.99897
1400	0.01806	0.3369	1.12398E-4	0.36589	0.9989
1600	0.01947	0.31769	1.10539E-4	0.33489	0.99923
1800	0.01525	0.31865	1.21026E-4	0.34943	0.99897
2000	0.01353	0.31518	1.27226E-4	0.35147	0.99902
2200	0.00652	0.32199	1.4046E-4	0.38433	0.99786
2400	0.00879	0.30057	1.26783E-4	0.35568	0.99879
2600	0.00456	0.30721	1.37892E-4	0.3795	0.99908
2800	0.0093	0.28809	1.27894E-4	0.35059	0.999

Table S6. Fitted parameters (χ_T, χ_S, τ and α) with the extended Debye model for the compound *M*-**1** at 1400 Oe in the temperature range 2-6.5 K. The fitting procedure applies only when the maximum is visible on χ_M'' vs ν.

T / K	χ_T / cm^3 mol^{-1}	χ_S / cm^3 mol^{-1}	τ / s	α	R^2
2	0.56141	0.04363	9.82182E-5	0.3222	0.99951
2.2	0.53612	0.0336	8.7888E-5	0.34284	0.99906
2.4	0.52108	0.01848	7.97055E-5	0.37983	0.99931
2.6	0.50971	0.00462	7.26894E-5	0.4148	0.99948
2.8	0.48358	0.00454	6.35146E-5	0.41591	0.99881
3	0.48803	0	6.35613E-5	0.44963	0.99833
3.2	0.46466	0.00117	5.59039E-5	0.44574	0.99847
3.4	0.44663	0.01527	5.39343E-5	0.42578	0.99843
3.6	0.42428	0.02883	5.04483E-5	0.40107	0.99797
3.8	0.40338	0.04986	4.94201E-5	0.35345	0.9981
4	0.38277	0.05933	4.47231E-5	0.32215	0.99808
4.2	0.35981	0.0754	4.12472E-5	0.26805	0.99796
4.5	0.33757	0.09088	3.75061E-5	0.20739	0.9981
5	0.3033	0.09474	2.78261E-5	0.14641	0.99859
5.5	0.27535	0.09938	2.13612E-5	0.09502	0.99933
6	0.2523	0.09776	1.60677E-5	0.06739	0.99967
6.5	0.2314	0.10866	1.40038E-5	0.00905	0.99936

S8 References

1 M. F. Richardson, W. F. Wagner and D. E. Sands, *J. Inorg. Nucl. Chem.,* 1968, **30**, 1275–1289.

2 A. Bedi, A. M. Armon, Y. Diskin-Posner, B. Bogosalvsky and O. Gidron, *Nat. Commun.*, 2022, **13**, 451-458.

3 G. M. Sheldrick, *Acta Crystallogr., Sect. A: Found. Adv.,* **2015**, *71*, 3–8.

4 G. M. Sheldrick, *Acta Crystallogr., Sect. C: Struct. Chem.,* **2015**, *71*, 3–8.

5 A. L. Spek, *J. Appl. Crystallogr.,* 2003, **36**, 7–13.

6 G. A. Bain and J. F. Berry, *J. Chem. Educ.,* 2008, **85**, 532-536.

7 K. Dhbaibi, M. Grasser, H. Douib, V. Dorcet, O. Cador, N. Vanthuyne, F. Riobé, O. Maury, S. Guy, A. Bensalah-Ledoux, B. Baguenard, G. L. J. A. Rikken, C. Train, B. Le Guennic, M. Atzori, F. Pointillart and J. Crassous, *Angew. Chem. Int. Ed*, 2023, **135**, e202215558.

8 G. te Velde, F. M. Bickelhaupt, E. J. Baerends, C. Fonseca Guerra, S. J. A. van Gisbergen, J. G. Snijders, T. Ziegler, *J. Comput. Chem.* 2001, **22**, 931-967.

9 E. van Lenthe, E. J. Baerends, J. G. Snijders, *J. Chem. Phys.* 1993*,* **99**, 4597-4610.

10 E. van Lenthe, A. Ehlers, E. J. Baerends, *J. Chem. Phys.* 1999, **110**, 8943-8953.

11 J. P. Perdew, K. Burke, M. Ernzerhof, *Phys. Rev. Lett.* 1996, **77**, 3865-3868.

12 J. P. Perdew, K. Burke, M. Ernzerhof, *Phys. Rev. Lett.* 1997, **78**, 1396.

13 E. van Lenthe, E. J. Baerends, *J. Comput. Chem.* 2003, **24**, 1142-1156.

14 B. O. Roos, P. R. Taylor, P. E. M. Sigbahn, *Chem. Phys.* 1980, **48**, 157-173.

15 I. F Galván, M. Vacher, A. Alavi, C. Angeli, F. Aquilante, J. Autschbach, J. J. Bao, S. I. Bokarev, N. A. Bogdanov, R. K. Carlson, L. F. Chibotaru, J. Creutzberg, N. Dattani, M. G. Delcey, S. S. Dong, A. Dreuw, L. Freitag, L. M. Frutos, L. Gagliardi, F. Gendron, A. Giussani, L. González, G. Grell, M. Guo, C. E. Hoyer, M. Johansson, S. Keller, S. Knecht, G. Kovačević, E. Källman, G. Li Manni, M. Lundberg, Y. Ma, S. Mai, J. P. Malhado, P. Å. Malmqvist, P. Marquetand, S. A. Mewes, J. Norell, M. Olivucci, M. Oppel, Q. M. Phung, K. Pierloot, F. Plasser, M. Reiher, A. M. Sand, I. Schapiro, P. Sharma,C. J. Stein, L. K. Sørensen, D. G. Truhlar, M. Ugandi, L. Ungur, A. Valentini, S. Vancoillie, V. Veryazov, O. Weser, T. A. Wesołowski,P.-O. Widmark, S. Wouters, A. Zech, J. P. Zobel and R. Lindh, *J. Chem. Theory Comput.* 2019, **15**, 5925-5964.

16 Li Manni, G. *et al. J. Chem. Theory Comput.* 2023, **19**, 6933-6991.

17 M. Douglas, N. M. Kroll, *Annals of Physics* 1974, **82**, 89-155.

18 B. A. Hess, *Phys. Rev. A* 1986, **33**, 3742-3748.

18 A. Wolf, M. Reiher, B. A. Hess, *J. Chem. Phys.* 2002, **117**, 9215-9226.

19 P.-O. Widmark, P.-Å. Malmqvist, B. O. Roos, *Theo. chimica acta* 1990, **77**, 291-306.

20 B. O. Roos, R. Lindh, P-Å. Malmqvist, V. Veryazov, P.-O. Widmark, *J. Phys. Chem. A* 2004, **108**, 2851-2858. +

21 B. O. Roos, R. Lindh, P.-A. Malmqvist, V. Veryazov, P.-O. Widmark and A.-C. Borin, *J. Phys. Chem. A*, 2008, **112**, 11431-11435.

22 F. Aquilante, P.-A. Malmqvist, T. B. Pedersen, A. Ghosh and B. O. Roos*, J. Chem. Theory Comput.*, 2008, **4**, 694-702.

23 K. Andersson, P.-Å. Malmqvist, B. O. Roos, A. Sadlej, K. Wolinski. *J. Phys. Chem.* 1990, **94**, 5483–5486.

24 K. Andersson, P.-Å. Malmqvist, B. O. Roos. *J. Chem. Phys.* 1992, 96, 1218–1226.

25 P. Å. Malmqvist, B. O. Roos, B. Schimmelpfennig, *Chem. Phys. Lett.* 2002, **357**, 230-240.

26 P.-Å. Malmqvist, B. O. Roos, *Chem. Phys. Lett.* 1989, **155**, 189-194.

27 B. A. Heß, C. M. Marian, U. Wahlgren, O. Gropen, *Chem. Phys. Lett.* 1996, **251**, 365-371.

28 L. F. Chibotaru, L. Ungur, *J. Chem. Phys.* 2012, **137**, 064112.

29 G. Kopnov, G. L. J. A. Rikken, *Rev. Sci. Instrum.* 2014, **85**, 053106.